Supplementary information

Facile microwave assisted synthesis of vastly edge exposed electrochemically 1T-MoS_2 for hydrogen evolution catalysis

Young Bum Lee[a,#], Seong K. Kim[a,#], Seulgi Ji[a], Wooseok Song[a], Hee-Suk Chung[b], Moon Kang Choi[c], Minbaek Lee[c], Sung Myung[a], Jongsun Lim[a], Ki-Seok An[a], and Sun Sook Lee[a,*]

[a]*Thin Film Materials Research Center, Korea Research Institute of Chemical Technology, Yuseong Post Office Box 107, Daejeon 305-600, Republic of Korea*

[b]*Analytical Research Division, Korea Basic Science Institute, Jeonju, Jeollabuk-do 54907, Republic of Korea*

[c]*Department of Physics, Inha University, Incheon 22212, Republic of Korea*

[#]These authors contributed equally to this work.

Corresponding Author

*E-mail: *sunsukl@krict.re.kr*

Reaction mechanism of hydrogen evolution and corresponding Tafel slopes

The main text mentions two different mechanisms of hydrogen evolution reaction. In case of platinum, the reaction follows Volmer-Tafel mechanism, while TMDs catalysts are known to follow Volmer-Heyrovsky mechanism. The chemical reaction equations showing each of the reaction steps of two mechanisms are shown below:

$$H^+(aq) + e^- \rightarrow H^{ad} \qquad \text{(Eq. 1; Volmer Reaction)}$$

$$H^{ad} + H^+(aq) + e^- \rightarrow H_2(g) \qquad \text{(Eq. 2; Heyrovsky Reaction)}$$

$$H^{ad} + H^{ad} \rightarrow H_2(g) \qquad \text{(Eq. 3; Tafel Reaction)}$$

For either mechanism, hydrogen evolution is considered to be rate-determined by Volmer reaction if Tafel slope is ~120 mV/dec. On the other hand, if the hydrogen evolution reaction is rate-determined solely by Heyrovsky reaction, Tafel slope of 40 mV/dec is expected. Lastly, in case of platinum, Tafel slope of ~30 mV/dec is observable since hydrogen evolution is now rate-determined by Tafel reaction.

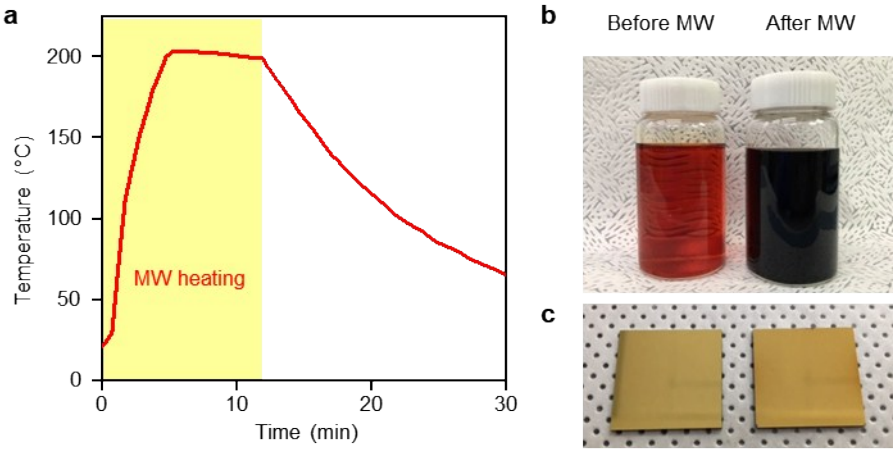

Figure S1. Microwave assisted synthesis and process. (a) Temperature profile with microwave heating. Reaction solution's temperature reaches to 200°C in three minutes of microwave annealing. Change in color for reaction solution (b) and gold substrate (c). Thin and uniform MoS_2-MW film was formed on the electrode surface without any precipitates or particles.

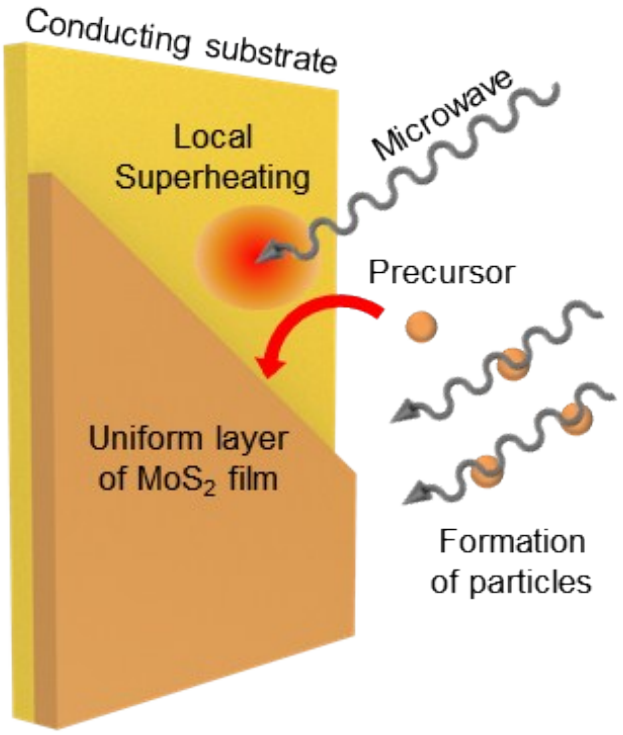

Figure S2. Scheme for synthesis mechanism of microwave assisted reaction. Microwave generates local hotspots which act as nucleation sites for reaction throughout the system. Local superheating near the metal surface leads to synthesize uniform layer of MoS_2 film with fast reaction rate regardless of morphology of the substrate.

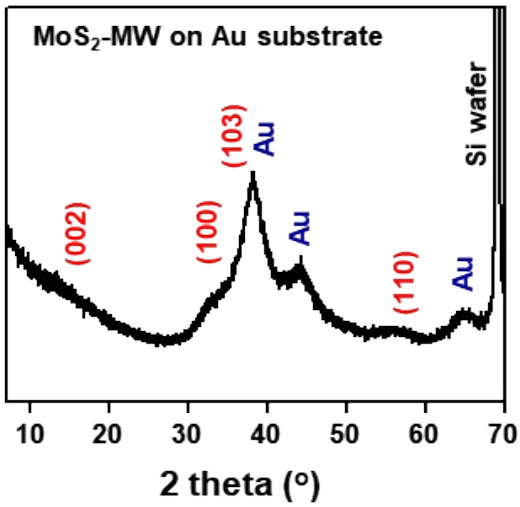

Figure S3. XRD measurement of MoS_2-MW (8 nm) on Au (50 nm)/SiO_2 (300 nm)/Si (001) substrate. Peaks from Au metal are strong while the MoS_2 thin film grown at low-temperature shows weak peak intensities.

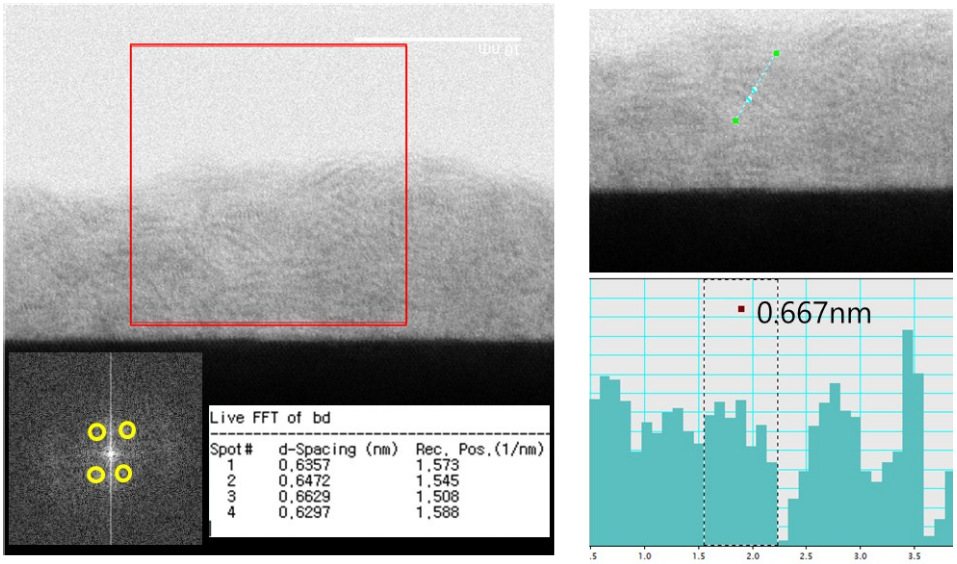

Figure S4. Interlayer distance measurement from STEM images. For statistical measurement of average d-spacing values, the fast Fourier transform (FFT) pattern of the STEM images which show various interlayer structures was utilized. The resulting d-spacing values ranging from 0.63 nm to 0.67 nm have in good agreement with the directly measured values.

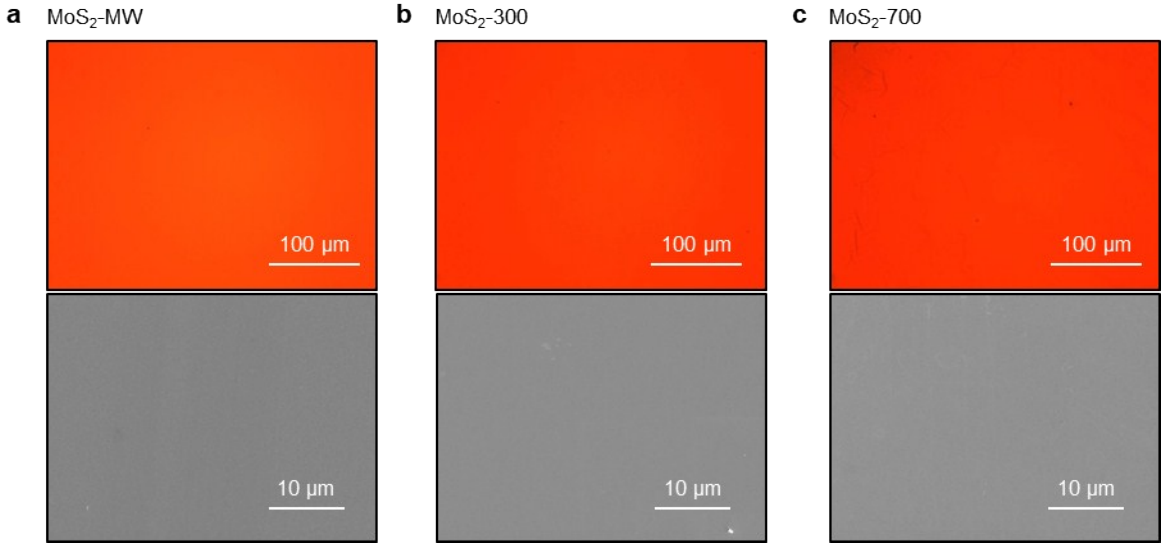

Figure S5. Surface morphology measurements using optical microscope and SEM. Optical microscopy images (top) and SEM images (bottom) for MoS_2-MW (a), MoS_2-300 (b), and MoS_2-700 (c) samples. MoS_2 films synthesized utilizing $(NH_4)_2MoS_4$ precursor form continuous and uniform film without any form of flakes.

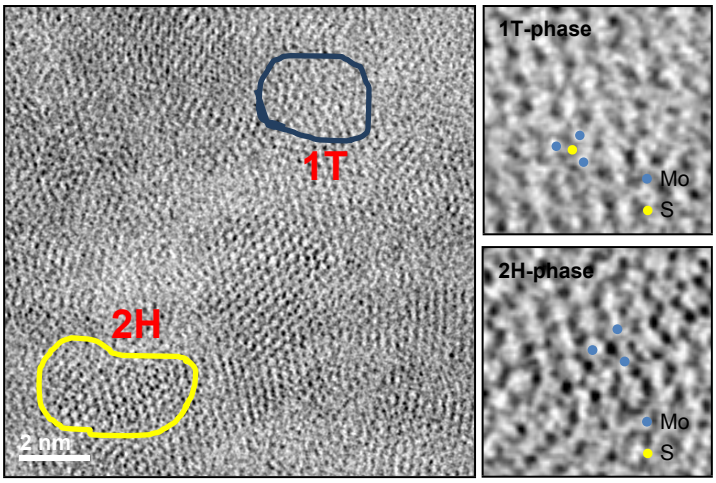

Figure S6. STEM image and atomic structure of MoS_2-MW which has randomly mixed in-plane heterostructure of 1T- and 2H-phases.

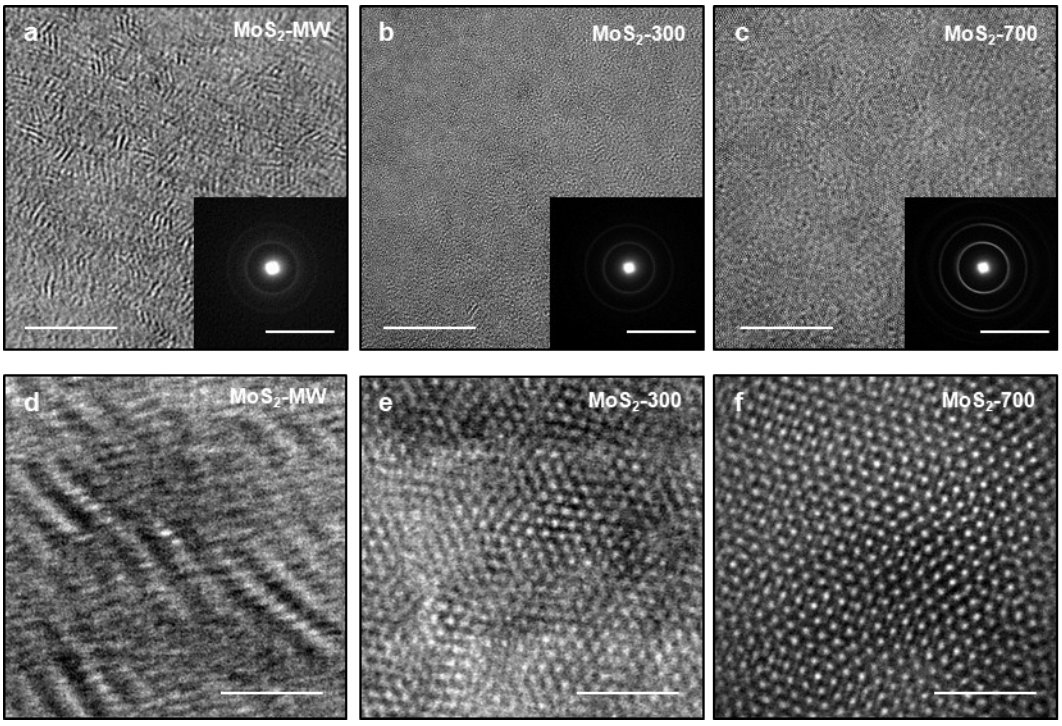

Figure S7. Atomic structure of bottom-up synthesized MoS_2. TEM measurements for MoS_2-MW (a), MoS_2-300 (b), and MoS_2-700 (c). Unlike MoS_2-300 and MoS_2-700 samples, MoS_2-MW sample has tilted grains within the layer (Scale bar, 10 nm), and insets show MoS_2 related SAED pattern regarding each sample. (Scale bar, 10 1/nm) Annular dark-field (ADF) images of the samples filtered by a local two-dimensional Wiener filter to enhance contrasts. Scale bar, 2 nm. MoS_2-MW (d) exhibits vertically-oriented grains whereas MoS_2-300 (e) and MoS_2-700 (f) show planar honeycombed grain structures.

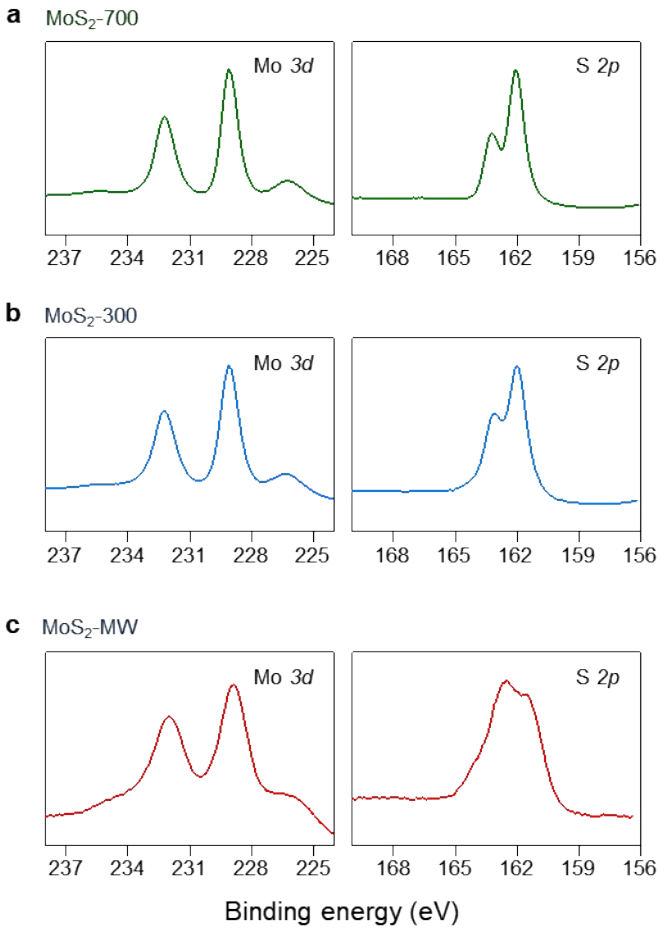

Figure S8. XPS core-level spectra without deconvolution for the three samples. Raw core-level spectra of molybdenum (left) and sulfur (right) obtained from MoS_2-700 (a), MoS_2-300 (b), and MoS_2-MW (c).

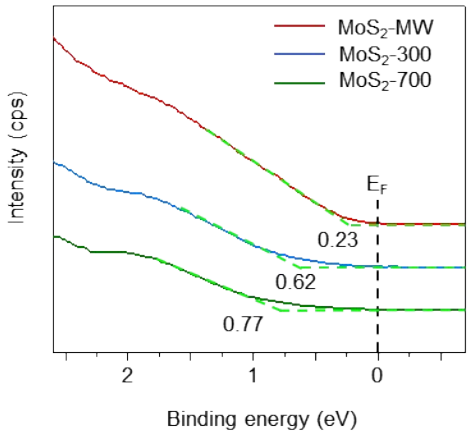

Figure S9. Valence band maximum spectra of MoS_2-700, MoS_2-300 and MoS_2-MW. The valence band maximum spectrum of MoS_2-MW is upshifted by 0.54 eV toward the Fermi level state compared to that of MoS2-700, which exhibits strong electron coupling of MoS2-MW sample.

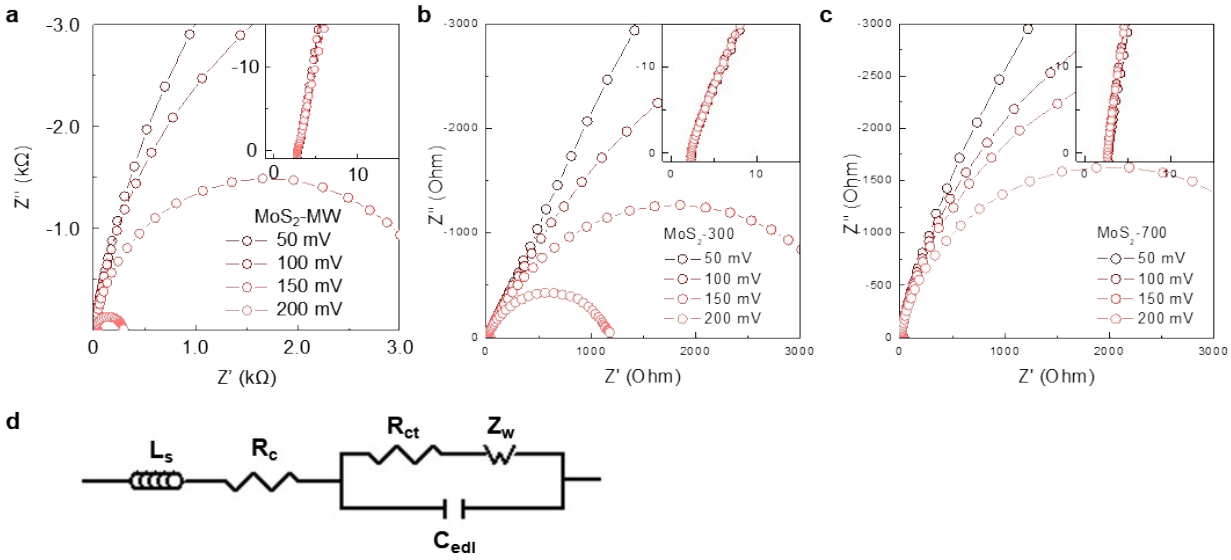

Figure S10. Nyquist plots of the three samples with a proposed equivalent circuit for analysis. The result of impedance measurement is shown as Nyquist plots for each sample (MoS_2-MW (a), MoS_2-300 (b), and MoS_2-700 (c)). A proposed equivalent circuit (d) for analysis of the result is shown.

Fig. S10 displays the Nyquist plots obtained from MoS_2-MW, MoS_2-300, and MoS_2-700 using the electrochemical ac-impedance spectroscopy (EIS) performed with applied dc-potential of 50, 100, 150, and 200 mV vs. RHE. The equivalent circuit consists of four serial elements, which are L_s, R_c, and a Warburg component (Z_w) to account for diffusion tied with another RC component for charge transfer (R_{ct}) in the electric double layer (C_{edl}). Here, L_s accounts for the inductive behavior of our measurement set-up, R_c symbolizes the resistance from cell (e.g. electrolyte resistance, electrode resistance, and ohmic contact resistance, etc), the Warburg element represents the resistance and capacitance from the diffusion of proton in electrolyte, the RC element represents the charge transfer resistance and C_{edl} electric double layer capacitance, respectively. The applied voltage independent cell resistances (inset) are considerably low, implying that factors hindering electron supply or ion transport can be neglected in electrochemical performance evaluation. As seen from Nyquist plots from MoS_2-

MW, MoS_2-300, and MoS_2-700, the mid-frequency semi-circle corresponding to diffusion of the protons in the electrolyte is almost non-existent demonstrating negligible diffusional resistances exist for all flat samples.

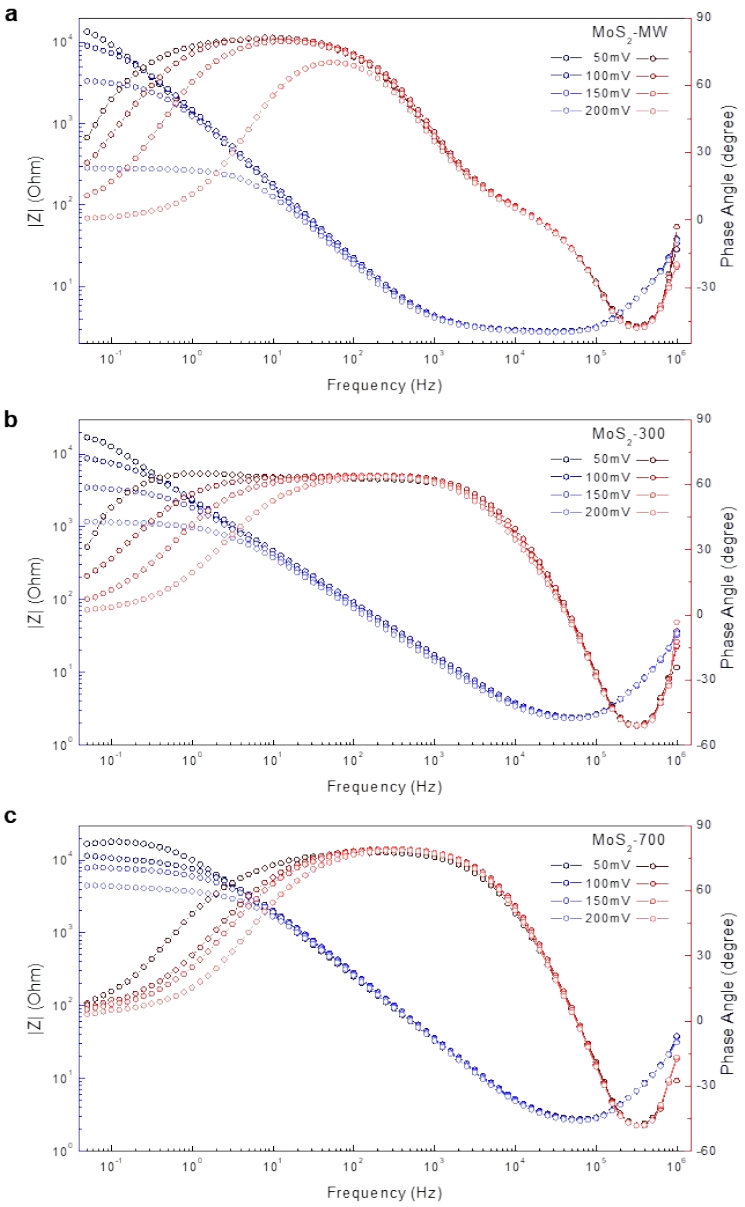

Figure S11. Bode plots obtained from impedance result of each sample. Small contribution from diffusional resistance can be observed only from MoS_2-MW (a) compared to MoS_2-300 (b) and MoS_2-700 (c). However, the diffusional resistance is, in fact, small enough to be neglected for all samples. (it is actually almost unobservable in Fig. S10).

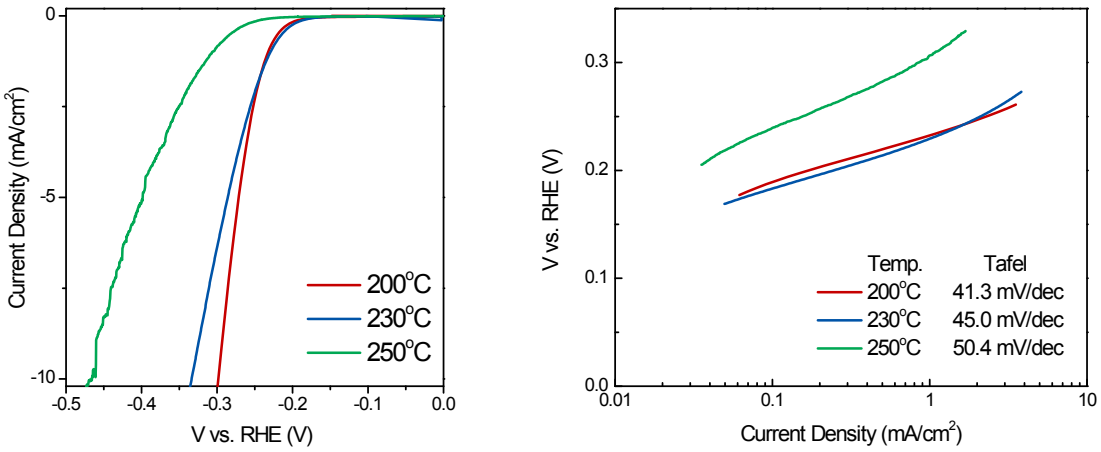

Figure S12. LSV and Tafel plots from the MoS_2-MW samples in different synthetic temperature.

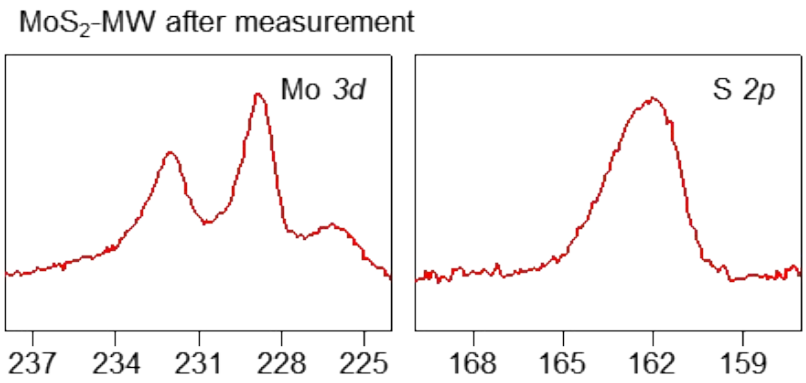

Figure S13. XPS core-level spectra of Mo and S atoms in MoS_2-MW sample after HER measurements.

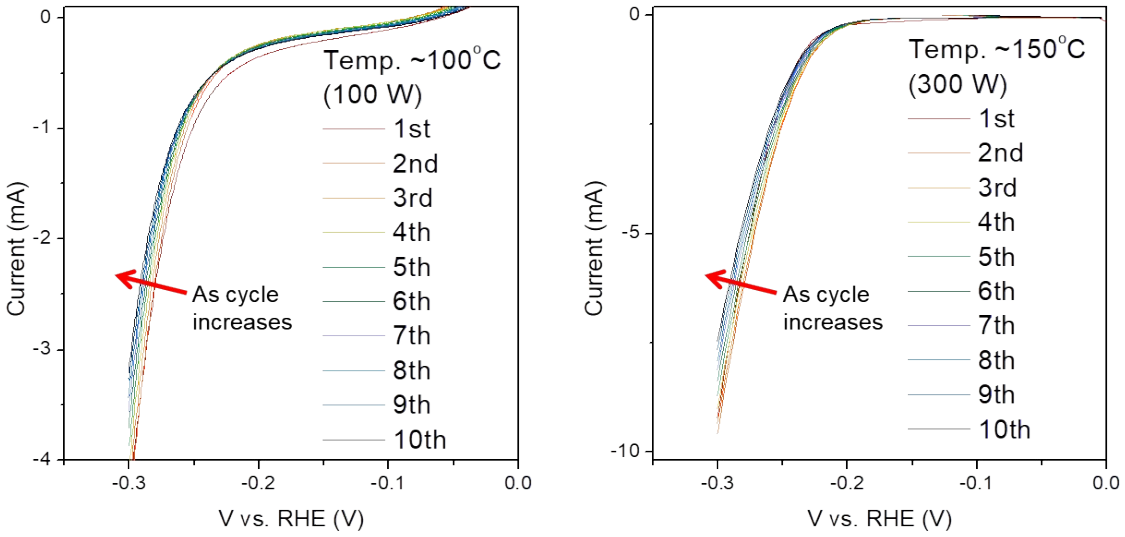

Figure S14. LSV stability tests from the MoS_2-MW samples which synthesized at the temperature below 200 °C.

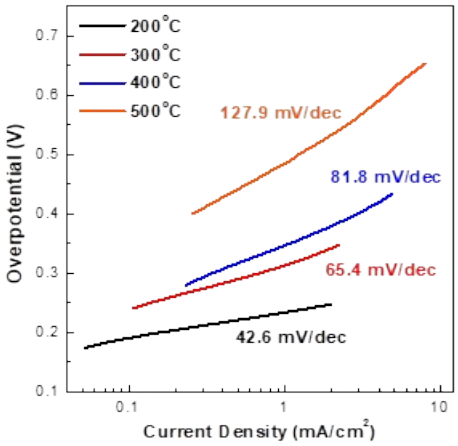

Figure S15. Tafel measurement for post-annealed MoS_2-MW samples with regard to different temperatures. Post-annealing temperature of 200°C (black), 300°C (red), 400°C (blue), and 500°C (orange) gives Tafel values of 42.6, 65.4, 81.8, and 127.9 mV/dec for each sample, respectively. As the annealing temperature becomes higher, metastable 1T-phase within the MoS_2-MW film gradually transform to 2H-phase yielding higher Tafel values.

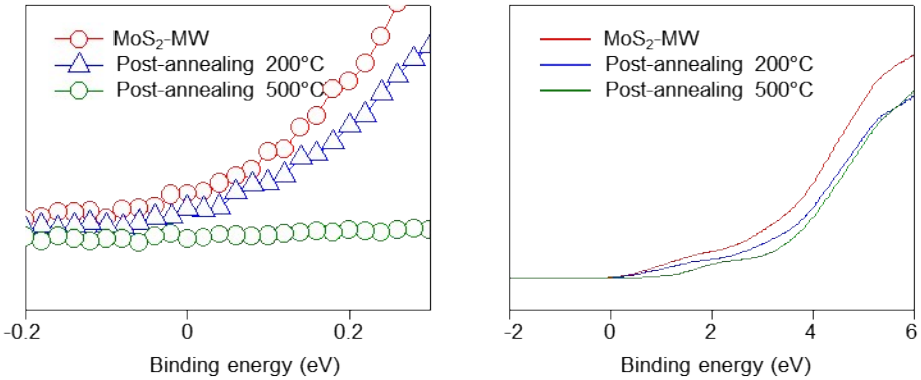

Figure S16. Valence Band Maximum data from UPS measurement for post-annealed samples. Valence band maximum spectra near the Fermi-level (left) and their full range spectrum (right). Post-annealed sample at 200°C (blue) has small decrease in density of state of MoS_2-MW (red) near the Fermi level, whereas post-annealed at 500°C (green) has little density of state at Fermi level.

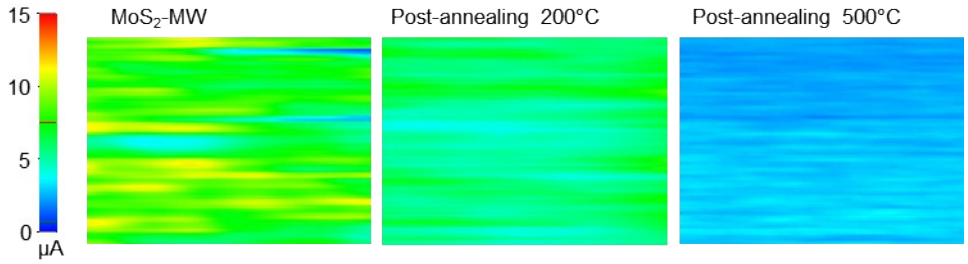

Figure S17. Conductive atomic force microscopy data for post-annealed samples. Post-annealing of 200°C of MoS_2-MW (middle) gives similar conductivity values of pristine MoS_2-MW (left), while post-annealing of 500°C of MoS_2-MW (right) shows significant decreased conductivity.

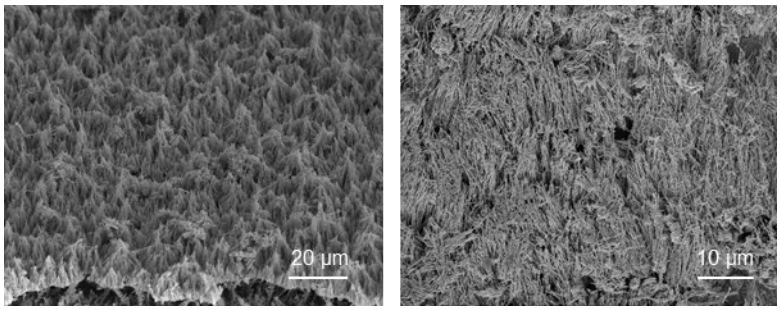

Figure S18. SEM images of MoS_2-MW coated on Au NWs. Tilted view of MoS_2-MW coated on Au NWs electrode (left) and image of the nanowire after physical pressing (right) to observe individual nanowires.

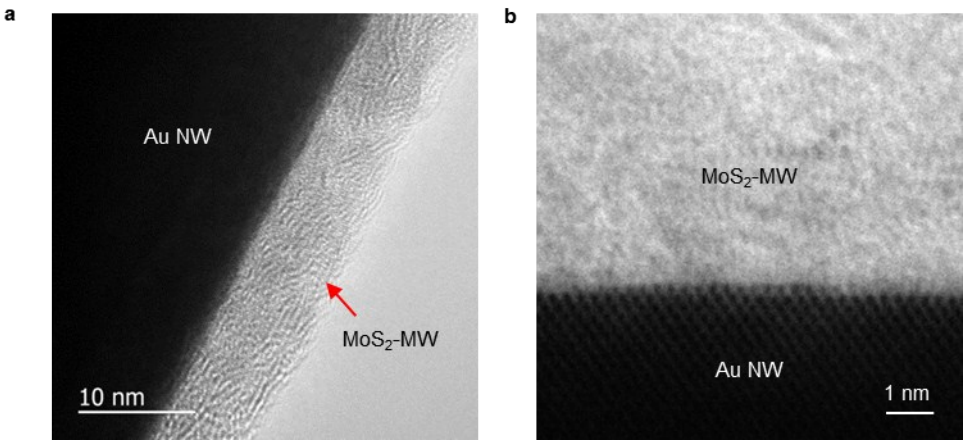

Figure S19. HRTEM and STEM images of single MoS_2-MW coated Au NW. (a) HRTEM images to observe interface and random orientation of MoS_2-MW grains. (b) Annular bright field STEM observation at the interface between Au NW and MoS_2-MW. The image shows clear interface between the layers without any Au atom diffusion.

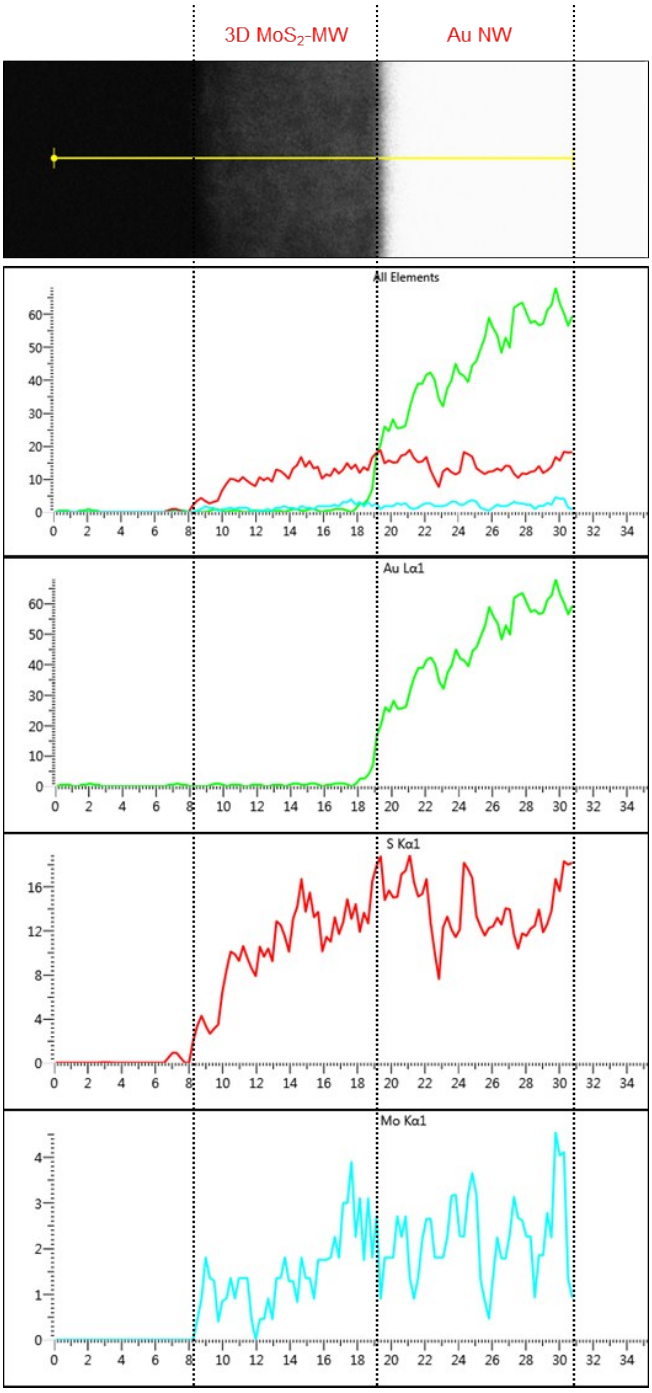

Figure S20. ADF-STEM images and EDS line scanning for MoS_2-MW coated Au NW. EDS signals of Au (green), S (red), and Mo (blue) shows uniform coating of MoS_2-MW on Au NW and clear interface between the layers.

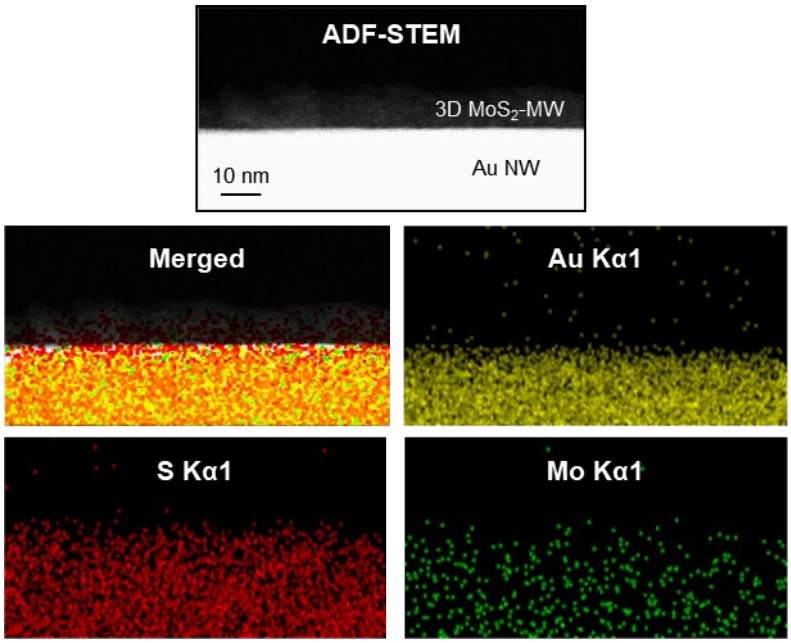

Figure S21. ADF-STEM images and EDS mapping for MoS_2-MW coated Au NW. ADF-STEM image of MoS_2-MW on Au NW (top) and EDS mapping results for Au (yellow), S (red), and Mo (green), and their merged images with ADF-STEM image confirms the structure of MoS_2 layer on Au NW.

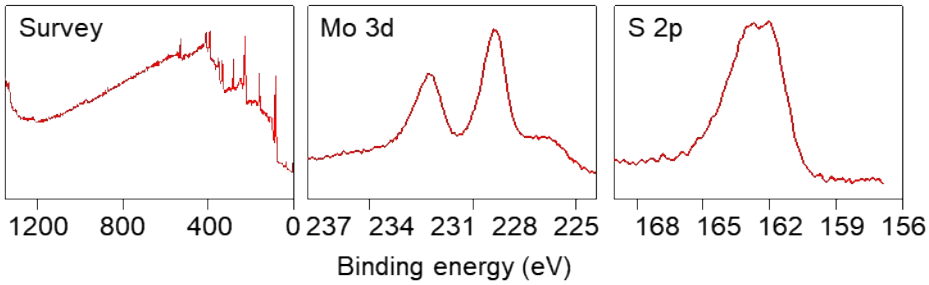

Figure S22. XPS core-level spectra for MoS_2-MW coated on Au NW. Survey spectrum (left) and core-level spectra of Mo 3d (middle) and S 2p (right), which has similar spectrum of flat MoS_2-MW sample.

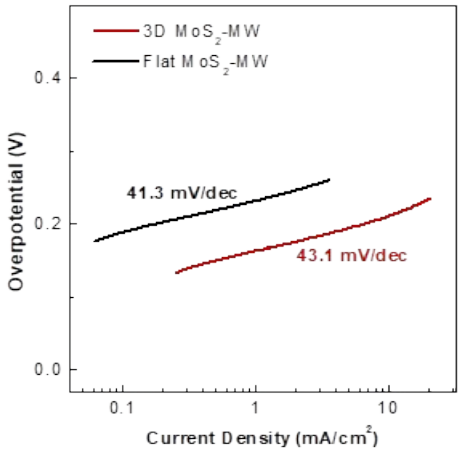

Figure S23. Tafel measurement for flat MoS_2-MW sample and 3D MoS_2-MW sample. Both flat (black) and 3D (red) MoS_2-MW samples show similar Tafel slopes (43.1 mV/dec and 41.3 mV/dec for 3D and flat samples, respectively) which indicates both electrodes involves same reaction mechanism for hydrogen evolution.

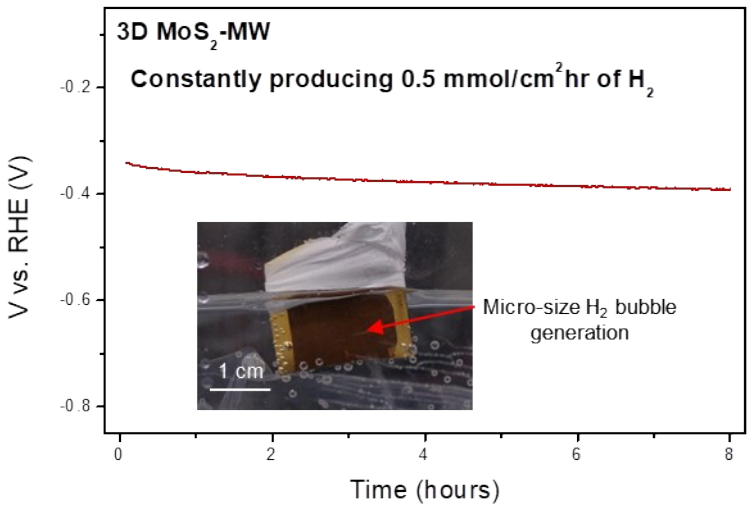

Figure S24. Stability of 3D MoS_2-MW upon continuous production of hydrogen. Stable and constant production of 0.5 mmol/cm^{2}hr of hydrogen by 3D MoS_2-MW was confirmed. Less than 0.05 V change was observed over continuous run of 8 hours. Inset is sample image that generates micro-sized hydrogen bubbles.

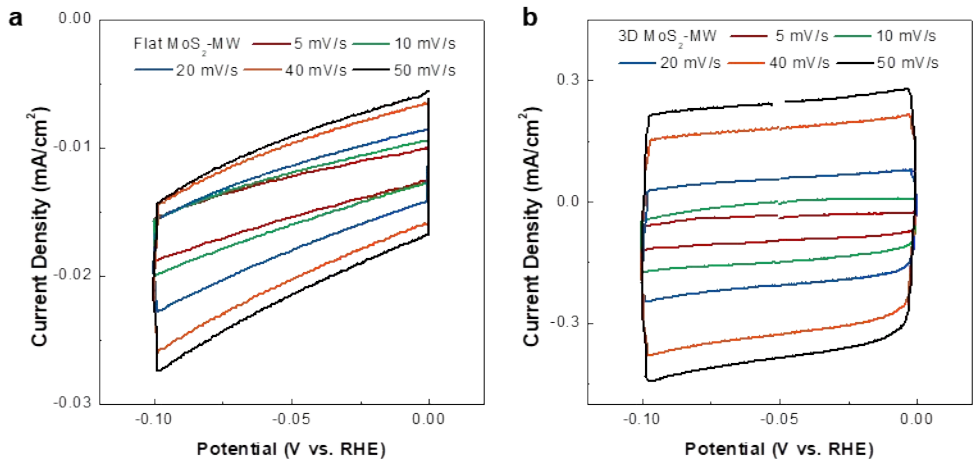

Figure S25. Cyclic voltammetry measurement for flat MoS_2-MW sample and 3D MoS_2-MW sample. Cyclic voltammetry spectra within non-faradaic region for flat (a) and 3D MoS_2-MW (b) samples with scan rate of 5, 10, 20, 40, and 50 mV/s.

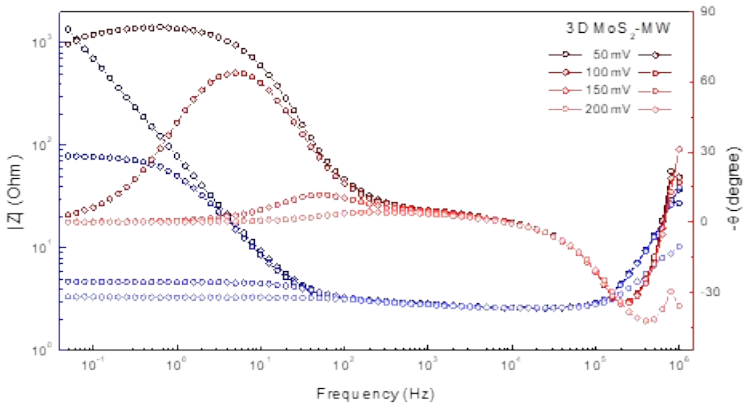

Figure S26. Bode plot attained from ac-impedance measurement with different bias-voltage applied. Voltages above 200 mV vs. RHE were also applied, but not plotted here because change is hard to observe above 200 mV vs. RHE.

Along with the Nyquist plot in Figure 4f, the Bode plot of 3D MoS_2-MW show a mid-frequency response related to diffusion of ions to electrode. Especially when high voltage (350 mV vs. RHE) was applied during the impedance measurement, the low frequency response corresponding to the electrode-electrolyte interface is almost completely reduced. Hence, the response related to diffusion at mid-frequency is well-exposed. Compared to flat MoS_2-MW, the diffusional resistance of 3D MoS_2-MW is slightly larger probably due to complex morphological structure of 3D MoS_2-MW hindering the diffusion of hydronium ions.

Materials	Methods	Morphology	On-set potential [mV]	Tafel [mV/dec]	Ref.
2H MoS_2	Bulk	Nanosheets	-350	117	[9]
1T MoS_2	Li^+	Exfoliated flakes	-200	41-46	[10]
1T MoS_2	Li^+	Flower-like MoS_2	-195	54	[9]
1T MoS_2	Li^+	Nanodots	-173	53	[47]
TiO_2/MoS_2	Li+	Nanosheet	-300	-	[22]
MoS_2/RGO	Solvothermal	Nanoparticles	- 150	41	[2]
MoS_2/graphene	Solvothermal	Vertical nanosheet	-176	41	[48]
CdS/1T-MoS_2	Solvothermal	Powder	>-300	98	[8]
1T/2H MoS_2	Solvothermal	Powder	-234	46	[19]
MoS_2-MW	Microwave	Dense Thin film	-290 (flat), -240 (3D)	41.3 (flat), 43.1 (3D)	Our work

Table S1. Electrocatalytic performance of various types of MoS_2 and composites.